


Please cite the Published Version

Mollah, Md Aslam, Sarker, Hasan, Ahsan, Mominul, Elahi, Md Towfik, Based, Md Abdul, Haider, Julfikar  and Palani, Sivaprakasam (2021) Designing Highly Sensitive Surface Plasmon Resonance Sensor With Dual Analyte Channels. IEEE Access, 9. pp. 139293-139302.

DOI: <https://doi.org/10.1109/access.2021.3118927>

Publisher: Institute of Electrical and Electronics Engineers (IEEE)

Version: Published Version

Downloaded from: <https://e-space.mmu.ac.uk/628577/>

Usage rights:  [Creative Commons: Attribution 4.0](https://creativecommons.org/licenses/by/4.0/)

Additional Information: This is an Open Access article published in IEEE Access.

Enquiries:

If you have questions about this document, contact openresearch@mmu.ac.uk. Please include the URL of the record in e-space. If you believe that your, or a third party's rights have been compromised through this document please see our Take Down policy (available from <https://www.mmu.ac.uk/library/using-the-library/policies-and-guidelines>)

Designing Highly Sensitive Surface Plasmon Resonance Sensor with Dual Analyte Channels

MD. ASLAM. MOLLAH¹, (Member, IEEE), HASAN SARKER¹, MOMINUL AHSAN², MD. TOWFIK ELAHI¹, MD. ABDUL BASED³, (Member, IEEE), JULFIKAR HAIDER⁴, and SIVAPRAKASAM PALANI⁵

¹Department of Electronics and Telecommunication Engineering, Rajshahi University of Engineering and Technology, Rajshahi-6204, Bangladesh (e-mail: ruet10aslam@gmail.com, hasan.ruet.ete@gmail.com, mntowfik15@gmail.com)

²Department of Computer Science, Deramore Lane, University of York, Heslington, York, YO10 5GH, UK

³Department of Electrical and Electronic Engineering, Faculty of Science and Technology, Dhaka International University, 66 Green Road, Dhaka-1205

⁴Department of Engineering, Manchester Metropolitan University, Chester St, Manchester M1 5GD, UK

⁵College of Electrical and Mechanical Engineering, Addis Ababa Science and Technology University, Addis Ababa, Ethiopia, P.O.Box 16417

Corresponding author: Sivaprakasam Palani (e-mail: shiva@aastu.edu.et)

ABSTRACT The ease of controlling waveguide properties through unparalleled design flexibility has made the photonic crystal fiber (PCF) an attractive platform for plasmonic structures. In this work, a dual analyte channel's highly sensitive PCF bio-sensor is proposed based on surface plasmon resonance (SPR). In the proposed design, surface plasmons (SPs) are excited in the inner flat portion of two rectangular analyte channels where gold (Au) strip is deposited. Thus, the surface roughness that might be generated during metal deposition on circular surface could be effectively reduced. Considering the refractive index (RI) change in the analyte channels, the proposed sensor is designed and fully characterized by the finite element method based COMSOL Multiphysics software. Improved sensing characteristics including wavelength sensitivity (WS) of 186,000 nm/RIU and amplitude sensitivity (AS) of $2,792.97 \text{ RIU}^{-1}$ in the wide RI range of 1.30 to 1.43 is obtained. In addition, the proposed sensor exhibits excellent resolution of 5.38×10^{-7} , signal to noise ratio (SNR) of 13.44 dB, figure of merits (FOM) of 2188.23, detection limit (DL) of 101.05 nm, and detection accuracy (DA) of 0.0204 nm^{-1} . Outcomes of the analysis indicate that the proposed sensor could be suited for accurate detection of organic chemicals, bio-molecules, and biological analytes.

INDEX TERMS plasmonic, bio-sensor, photonic crystal fiber, finite element method, detection limit

I. INTRODUCTION

THE high demand of portable, lightweight, high-resolving, and cost-effective devices for bio-sensing application has drawn immense interest in designing miniaturized sensors. The photonic crystal fibers (PCFs) possess excellent guiding properties, miniaturized size, lightweight, design freedom, etc [1]. On the other hand, a unique optical phenomenon surface plasmon resonance (SPR) offers high-sensitive, real-time and label-free sensing devices [2]. Hence, a combination of PCF and SPR are extensively used for numerous sensing applications that include bio-sensing, organic chemical sensing, gas sensing, environment observation, and so on [3]. In SPR, an electromagnetic (EM) wave called surface plasmon wave (SPW) is generated at the metal-dielectric interface when the free electrons of the metal become excited

by the evanescent wave of p-polarized light. A coupling occurs when the frequency of the incident photon and free electrons matches [4]. The coupling condition is highly sensitive to the surroundings; refractive index (RI) is one of them. Therefore, any small change in the surrounding's RI potentially changes the resonance or coupling conditions. Hence, an unknown analyte can be simply identified by observing a shift in the resonance peak.

To ensure the desired performance of any SPR sensor in practice, the suitable plasmonic metal selection is crucial. Most of the plasmonic applications rely on the noble metals (silver, gold, copper, aluminum) which exhibit a relatively low optical loss in the visible (380-760 nm) and near-infrared (750-2,500 nm) spectral regions [5]. From the perspective of optical characteristics, silver would be an attractive candi-

date in plasmonics, since it has low optical damping, very high conductivity, and insignificant inter-band transitions [6]. However, silver easily forms brittle oxide layers in the aqueous environment, making it inconvenient for sensing application. Although, aluminum has intrinsic high electron density [7], it possesses several disadvantages that include higher damping, and corrosion problems. Copper is cheaper than other metals, and the performance is acceptable as well but it also suffers from corrosion problems, even in atmospheric conditions it easily oxidizes and forms copper oxide (Cu_2O and CuO) layer [8]. Gold is an extensively used plasmonic metal despite having comparatively high optical damping since it is intrinsically inert, bio-compatible, chemically stable, and easy-to-structure [5].

Although SPR PCF sensor shows the immense potential for numerous applications particularly in bio-sensing, has some limitations associated with metal film deposition. Shuai *et al.* proposed a liquid core PCF having an internal circular air hole coated with gold and achieved a negative wavelength sensitivity (WS) of -5500 nm/RIU in the analyte range of 1.50-1.53 [9]. Later on, Gao *et al.* designed a Ge-doped solid silica core PCF having six internal circular air holes coated with thin gold and TiO_2 films and obtained WS and amplitude sensitivity (AS) of 2000 nm/RIU and 370 RIU⁻¹, respectively, in the relatively lower analyte range of 1.33 to 1.35 [10]. It can be noticed that the above-mentioned sensors possess very low sensing performance in terms of their sensitivity. Recently, Rifat *et al.* achieved improved sensitivity (AS and WS of 1,420 RIU⁻¹ and 11,000 nm/RIU, respectively) and wider sensing range (1.33 to 1.42) using only one gold-coated circular air hole [11]. However, internally metal deposition around a circular air hole is considered highly challenging. Hence, as an alternative, a lot of sensors have been demonstrated with externally metal deposited PCF [12]–[15]. For instance, a twin-core PCF having AS and WS of 1,085 RIU⁻¹ and 9,000 nm/RIU, respectively, is proposed by Paul *et al.* [12]. Islam *et al.* designed an SPR PCF sensor in the visible to the near-infrared spectral region and attained a reasonable maximum WS of 62000 nm/RIU [13]. Alphabetic-core assisted PCF SPR sensor having WS of 12,000 nm/RIU is proposed by Haider *et al.* in the analyte range of 1.33 to 1.40 [14]. Very recently, we have proposed a slotted PCF SPR sensor with an improved AS of 1,782.56 RIU⁻¹ [15]. However, the entire circular outer surface of the PCF of the above mentioned sensors is proposed to be covered by metal which causes an increase in surface roughness that would deteriorate the sensing performance [16], [17]. There are several methods of metal deposition that include chemical vapor deposition (CVD), thermal evaporation, vacuum evaporation, wet-chemistry deposition, RF sputtering, and atomic layer deposition (ALD). Nevertheless, none of these methods offer guaranteed uniformity of metal film on a circular surface [16]. To resolve this problem, a D-shaped PCF is developed where metal deposition takes place on a polished flat surface. Gangwar *et al.* demonstrated a gold-coated D-shaped PCF sensors with WS of 7,700

nm/RIU [18]. Chen *et al.* improved WS up to 11,055 nm/RIU for sensor operating wavelength from 2.9 to 3.6 μm [19]. Recently, Meng *et al.* achieved a relatively high WS of 29,000 nm/RIU but the sensing range was comparatively low of 1.377 to 1.385 [20]. However, D-shaped PCF requires perfect polishing after fabrication, which increases complications, and any disparity during polishing greatly influences the sensor performance. Moreover, the PCF becomes weaker and more fragile due to the polishing.

In this paper, a SPR sensor where the metal deposited internally at the inner flat surface of two analyte channels has been proposed. Hence, this design concept eliminates any additional polishing which is needed in the D-shaped sensor and reduces the possibility of imparting surface roughness which usually occurs during the deposition of metal coating on a circular surface. The proposed sensor is systematically optimized and physical explanation of each designed geometry is appropriately addressed. Moreover, superiority of the proposed sensor was demonstrated by evaluating the sensing performance in terms of WS, resolution, AS, linearity, figure of merit (FOM), signal to noise ratio (SNR), detection limit (DL) and detection accuracy (DA).

II. SENSOR STRUCTURE DESIGN, FABRICATION FEASIBILITY ANALYSIS, AND NUMERICAL MODELING

The sensor design and numerical analysis were performed using the finite element method (FEM) based commercially available COMSOL Multiphysics software. Wave optics module with Electromagnetic Waves Frequency Domain (EWFD) solver was employed to evaluate the guiding characteristics of the proposed PCF. Physics controlled mesh sequence with extremely fine element size was used that includes total mesh area of 654.1 μm^2 , total triangular element of 18,134, edge elements of 1448, vertex elements of 124, minimum element quality of 0.7785, average element quality of 0.9467, and element area ratio of 1.682×10^{-4} . The 2D view of the proposed sensor is illustrated in Figure 1(a). The cladding of the fiber consisted of two air holes with different diameters arranged in hexagonal lattice. In the first ring, comparatively smaller air holes (d) were used that ensured adequate light leaking from the core mode so that strong interaction could happen between the core and SPP mode. In the second and third ring, large air holes (D) were used to reduce the unwanted loss along the y-axis. On the other hand, two rectangular air holes on either side of the core were created for the analyte channels. The motivation for the rectangular air holes originated from the complexity of metal deposition on a circular surface.

The RI of the fiber material (SiO_2) is calculated as [21],

$$\eta(\lambda) = \sqrt{1 + \frac{M_1\lambda^2}{\lambda^2 - N_1} + \frac{M_2\lambda^2}{\lambda^2 - N_2} + \frac{M_3\lambda^2}{\lambda^2 - N_3}}, \quad (1)$$

where, λ = wavelength in μm and $\eta(\lambda)$ = effective RI of fused silica at λ , $M_1 = 0.696263$, $M_2 = 0.4079426$, $M_3 = 0.8974794$, $N_1 = 0.0046914826 \mu m^2$, $N_2 = 0.0135120631$

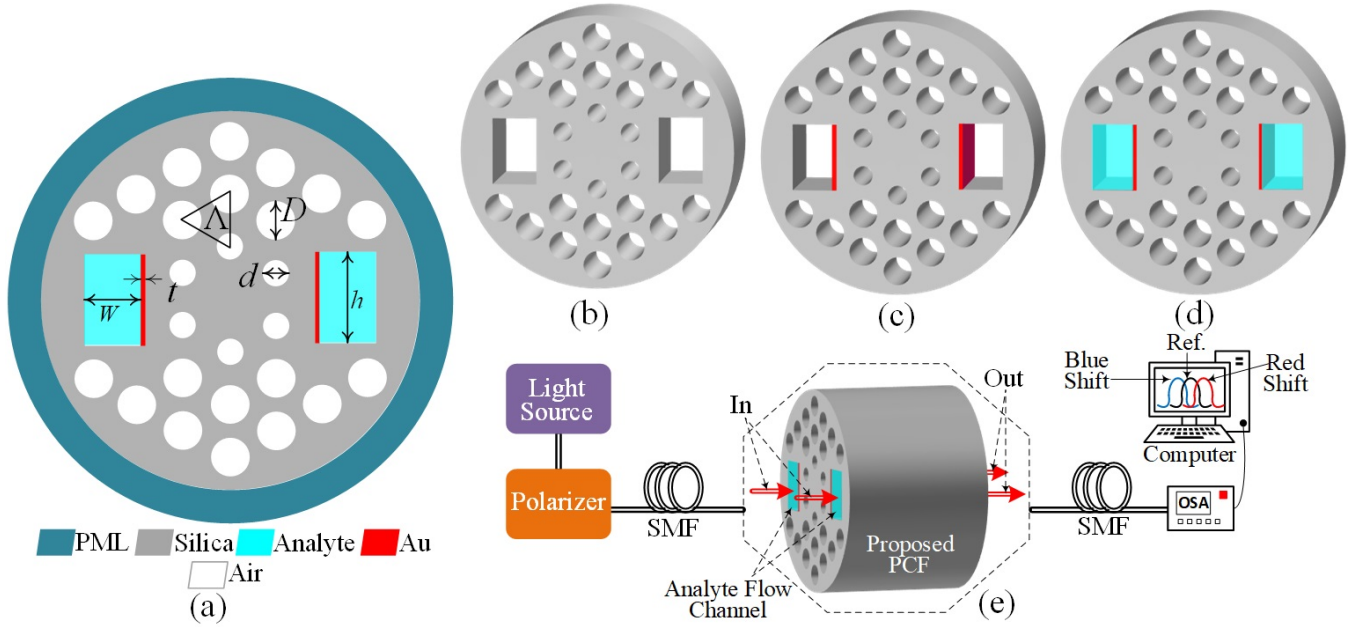


FIGURE 1: (a) 2D view of the proposed sensor, (b) 3D view of the PCF, (c) after metal coating on the inner flat portion of the analyte channel, (d) both channel is filled with analyte, and (e) generalized set up of analyte sensing practically using the proposed sensor. (PML: perfect matched layer; SMF: single mode fiber; OSA: optical spectrum analyzer; PCF: photonic crystal fiber).

μm^2 and $N_3 = 97.9340025 \mu\text{m}^2$ are known as Sellmeier's constants.

The gold film was placed on the inner flat surface of the rectangular air hole so that the evanescent wave could easily interact with the metal film. The wavelength dependent dispersion of gold is calculated from the Drude-Lorentz formula [22],

$$\varepsilon_G(\omega) = \varepsilon_\alpha - \frac{\omega_D^2}{\omega(\omega + i\gamma_D)} + \frac{\Delta_\epsilon \Omega_L^2}{(\omega^2 - \Omega_L^2) + i\Gamma_L \omega}, \quad (2)$$

where Γ_L = spectral width of the Lorentz oscillators, Δ_ϵ = 1.09 (known as weight factor), Ω_L = strength width of the Lorentz oscillators, γ_D = damping coefficient, $\omega_D = \frac{2\pi c}{\lambda}$ (known as plasma frequency), c = the velocity of light and ε_α = permittivity at high frequency with a value of 5.9673. Again, the values of the above parameters are: $\frac{\omega_D}{2\pi} = 2113.6$ THz, $\frac{\gamma_D}{2\pi} = 15.92$ THz, $\frac{\Gamma_L}{2\pi} = 104.86$ THz and $\frac{\Omega_L}{2\pi} = 650.07$ THz.

However, each design parameters have a significant impact on the confinement loss (CL) and the resonance wavelength shifting, which is briefly described in section III.

Fabrication of the proposed sensor can be carried out in two steps. Firstly, the PCF can be developed by drilling a fused silica rod using an ultrasonic mill [23], [24]. The computer numerical controlled (CNC) drilling machine has the ability to produce any shape of air hole with high precision through the controlling of the drilling parameters such as cutting speed, depth of cut, and spindle speed [25]. The final step, which is the most challenging, is the metal

deposition process. Fang *et al.* pictorially described how the metal deposition on the inner portion of the analyte channel can be carried out [24]. According to Fang *et al.*, just keeping a void for the metal at the inner portion, the whole rectangular slot (analyte channel) of the proposed sensor can be filled with polymethyl methacrylate (PMMA) by micro-machining operation technology. Then, the void can be filled with the metal through high-pressure microfluidic chemical deposition [26]. Lastly, the PMMA can be removed with acetone followed by channel rinsing with methanol and the channels can be dried by using a compressed air or nitrogen stream [27]. It should be noted that Boehm *et al.* experimentally demonstrated the metal deposition in the interior surfaces of a PCF through Tollens reaction [28]. Zhang *et al.* achieved selective air hole coating with metal by suction and evaporation of metal nanoparticle mixtures [29]. In addition, metal coated PCFs have been reported with fabrication techniques including sputtering [30], electroless plating [31], and thermal evaporation for tapered PCFs [32]. Though it remains a challenge to maintain uniformity and thickness of the metal coating inside and outside of the PCFs for sputtering and evaporation techniques, better uniformity of metal layers was achieved using chemical deposition methods with more complicated conditions, e.g., high pressure or high temperature [3]. However, substantial development has already been made in the field of metal coating process and the efforts are still continuing. Hence, in recent times, many works have been reported for the sensing performance improvement of the internally metal coated PCF

[33], [34]. The authors are optimistic that the advancement of the coating techniques will make the realization of internally metal coated PCFs including this proposed sensor with the required coating uniformity and thickness.

A straightforward set-up for experimental RI sensing using PCF sensor is depicted in Figure 1(e). An optical tunable source (OTS) can be used to achieve the optical power which is then launched into the single mode fiber (SMF) after being propagated through a polarizer so that single polarized light can be attained to introduce into the proposed PCF sensor. Any recently developed splicing technique can be used to achieve the coupling between the SMF and the proposed sensor. Note that two rectangular analyte channels of the proposed PCF sensor can be filled and cleaned through pumping. Here, In and OUT just indicates the in and out path of the liquid analyte. However, due to the change in the analyte, a significant change in the effective index of the surface plasmon polariton (SPP) mode happens leading to the resonance wavelength shifts either longer (red shift) or shorter (blue shift) wavelength. The transmitted optical power can be measured using an optical spectrum analyzer (OSA), which is connected with another SMF. Finally, the change of resonance wavelength shift could be observed and analyzed using a computer.

CL of the proposed sensor can be calculated by the following equation [35],

$$L_c \approx 8.686 \times k_0 \times \text{Im}(\eta_{eff}) \times 10^4 \text{ dB/cm}, \quad (3)$$

where, $\text{Im}(\eta_{eff})$ is the imaginary value of the refractive index, $k_0 = 2\pi/\lambda$ is the wave number in the free space and λ is the wavelength in μm .

The main features of the PCF-SPR sensor, WS, is measured by the wavelength interrogation method [36],

$$WS \text{ (nm/RIU)} = \frac{\Delta\lambda_{peak}}{\Delta n_a}, \quad (4)$$

where, $\Delta\lambda_{peak}$ is the shift of the peak in nm due to the variation of the RIU Δn_a .

The corresponding sensor resolution is evaluated as follows [37],

$$R \text{ [RIU]} = \frac{\Delta n_a \times \Delta\lambda_{min}}{\Delta\lambda_{peak}}, \quad (5)$$

where, Δn_a = change in analyte's RI, $\Delta\lambda_{min}$ = minimum spectral resolution and $\Delta\lambda_{peak}$ = peak shift of resonant wavelength. In this case the sensor resolution is calculated for $\Delta n_a = 0.01$ and $\Delta\lambda_{min} = 0.1 \text{ nm}$.

Another significant performance feature, AS, is evaluated by the amplitude interrogation method [13], [38],

$$AS \text{ (RIU}^{-1}\text{)} = -\frac{\Delta\alpha_{loss}}{\Delta n_a} \times SL = -\frac{\Delta\alpha_{loss}}{\Delta n_a \alpha_{neff}}, \quad (6)$$

$$SL = \frac{1}{\alpha_{neff}}, \quad (7)$$

where, SL denotes the sensor length, α_{neff} is the CL for a RI. Again $\Delta\alpha_{loss}$ is the loss variation in between two

adjacent RI of analytes and maximum AS locates at the resonant peak shift of wavelength.

Moreover, some special features e.g., FOM, SNR, DL, and DA, are calculated which are directly involved with the full width half maxima (FWHM) of the loss spectra [24], [39],

$$FOM = \frac{WS}{FWHM}, \quad (8)$$

$$SNR = \frac{\Delta\lambda_{peak}}{FWHM}, \quad (9)$$

$$DL = \frac{FWHM}{1.5 \times (SNR)^{0.25}}, \quad (10)$$

$$DA = \frac{1}{FWHM \text{ (nm)}}, \quad (11)$$

where, WS is the wavelength sensitivity and $\Delta\lambda_{peak}$ is the wavelength difference between two loss peaks.

III. PERFORMANCE CONTROLLING PARAMETERS AND OPTIMIZATION

All the geometrical parameters of the sensor have significant impact on the performance. Hence, before going to investigate the sensor performance, all of the designed parameters are optimized in a systematic way.

A. VARIATION OF GOLD LAYER THICKNESS

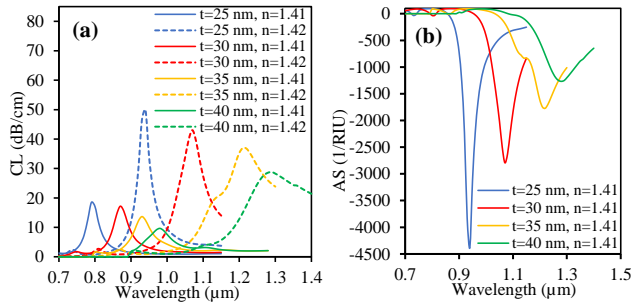
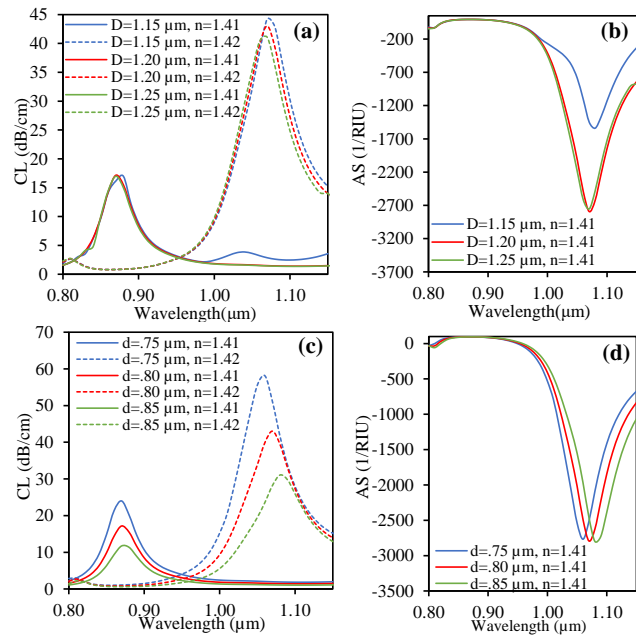
The thickness of gold layer (t) is crucial and influences the performance greatly. Here, t is varied from 25 nm to 40 nm with an increment of 5 nm, and the performance of the proposed sensor is investigated while keeping the other parameters undisturbed. The CL change with variation in t is shown in Figure 2(a) and WS is obtained from the numerical analysis which is summarised in Table 1. It is observed that with the increase of t , the peak value of CL is decreased due to the damping effect of gold [13] and the resonance peak is shifted to the longer wavelength. Though higher WS is achieved with thicker t , the resonance peak became wider which leads to lower AS and FOM. From Figure 2(b), it can be concluded that AS and FOM increase with the decreasing t that enhances the detection accuracy of the sensor. However, to make a trade off among WS, AS and FOM, 30 nm is chosen as an optimum thickness of t .

B. VARIATION OF AIR HOLE DIAMETER

There are two different sizes of air hole used in this design. The larger air hole with a radius of D and the smaller one with a radius of d are shown in Figure 1(a). Here, the impact of air hole size is analyzed in case of WS and AS and only a single parameter is varied each time as before. At first the air hole radius D is varied from 1.15 μm to 1.25 μm with an increment of 0.05 μm which is shown in Figure 3(a). Small change in the WS is observed when the D is changed from 1.15 μm to 1.20 μm . Although the loss peak

TABLE 1: Performance Analysis of the Proposed Sensor for Different Analyte RI With $\Delta n_a = 0.01$, $t = 30$ nm at Y-Polarized Mode.

Parameter	Quantity	FWHM (nm)	Peak CL (dB/cm)	Peak WS (nm/RIU)	Peak AS (RIU^{-1})	FOM (RIU^{-1})
gold thickness, t (nm)	25, 30, 35, 40	43.8, 53.7, 64, 90	18.466, 17.166, 13.642, 9.639	15000, 20000, 28000, 31000	-4380, -2790, -1770.98, -1267.48	342.47, 372.44, 437.5, 344.44
large air hole diameter, D (μm)	1.15, 1.20, 1.25	54, 52, 51.5	16.96, 17.17, 16.99	19000, 20000, 20000	-1539.86, -2792.97, -2753.42	351.85, 384.62, 388.35
small air hole diameter, d (μm)	0.75, 0.8, 0.85	51, 52.5, 55	23.99, 17.17, 11.72	19000, 20000, 21000	-2767.59, -2792.97, -2799.25	372.55, 380.95, 381.81
pitch, Λ (μm)	3.3, 3.4, 3.5	59, 52.5, 54	16.06, 17.17, 18.05	19000, 20000, 21000	-3007.2, -2792.97, -2565.29	322.03, 380.95, 388.89
analyte channle's height, h (μm)	5.9, 6.0, 6.1	52, 52.5, 53	17.32, 17.17, 17.06	20000, 20000, 20000	-2916.38, -2792.97, -2662.25	384.61, 380.95, 377.35
analyte channle's width, w (μm)	3.9, 4, 4.1	55, 52.5, 51.5	16.46, 17.17, 16.05	21000, 20000, 20000	-2853.89, -2792.97, -2705.46	381.81, 380.95, 388.35

FIGURE 2: Effect of gold layer thickness (t) on (a) CL, and (b) AS, of the proposed sensor considering RI = 1.41 and 1.42.FIGURE 3: Effect of air hole diameter on CL and AS, D (a-b), and d (c-d), considering RI of 1.41 and 1.42.

is found at different wavelength for 1.20 μm and 1.25 μm , due to same wavelength difference between the loss peak for the RI of 1.41 and 1.42, the WS is same. Figure 3(b), depicts corresponding AS and it can be observed that AS remains quite similar for D of 1.20 μm and 1.25 μm , but it changes significantly when the D is decreased from 1.20 μm to 1.15 μm . Considering the above parameters, $D = 1.20$ μm is chosen as an optimal value.

The same process is followed for d and the above optimized parameter as well as the other parameters are considered constant. d is varied from 0.75 μm to 0.85 μm with a step size of 0.05 μm . Figure 3(c) shows the corresponding CL curve and peak value (dB/cm) of the CL is summarized in Table 1. It can be observed that smaller d provides larger space to leak the light out of the core. As a result, higher CL is found with lower d . On the other hand, WS is increased to 1000 nm/RIU when the d is changed from 0.75 μm to 0.80 μm and there is no change obtained for any further increment. Figure 3(d) represents the AS for RI = 1.41, though AS changes are small, it increases with the increment of d . Considering the above parameters, $d = 0.80$ μm is chosen as a trade-off among WS, AS, FWHM and FOM.

C. VARIATION OF PITCH

The effect of pitch variation on the CL peak value and resonance wavelength shift is discussed for evaluating the performance of the proposed sensor. Figure 4(a) shows the CL curve for RI of 1.41 and 1.42 where the pitch (Λ) is varied from 3.3 μm to 3.5 μm with a step size of 0.1 μm . The resonance point of CL curve shifts to longer wavelength with the lower pitch than the higher one for RI = 1.42 and remain constant for RI = 1.41. However, every time the WS is increased to 1000 nm/RIU with the increment of Λ by 0.1 μm . In contrast, the AS decreases as the Λ increases which can be seen from Figure 4(b). On the other hand, from Table 1, it can be observed that FOM increases with the increment of Λ . Here, Λ is taken as 3.4 μm for maintaining a balance among the all-performance parameters.

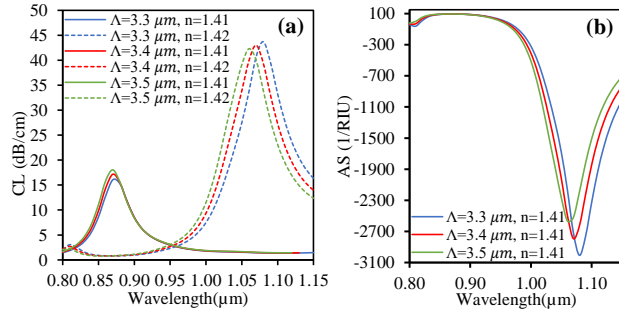


FIGURE 4: (a) CL, and (b) AS variation of the proposed sensor with pitch (Λ), considering RI of 1.41 and 1.42.

D. VARIATION OF HEIGHT AND WIDTH OF THE ANALYTE CHANNEL

The effect of the variation of the height (h) and width (w) of the analyte channel on the sensing performance is investigated. Figure 5(a) shows the CL curve with different values of h for RI of 1.41 and 1.42 and it is clearly seen that there is no change of the resonance wavelength with the h variation either for 1.41 or 1.42, although the peak value of CL point is slightly changed. Figure 5(b) represents the corresponding AS for RI = 1.41 and it can be observed that higher AS can be obtained with lower value of h . However, small analyte channel can increase the difficulty of metal deposition and analyte filling. Hence, we chose $h = 6 \mu\text{m}$ as an optimum height of the analyte channel.

The CL variation and AS with different value of w is plotted in Figure 5(c), and (d), respectively. It can be seen that higher WS as well as AS is obtained with lower value of w . However, considering the analyte filling and metal deposition difficulties, $w = 4 \mu\text{m}$ is chosen as the optimum width of the analyte channel.

IV. PERFORMANCE ANALYSIS WITH NUMERICAL RECORDS

Figure 6(a) represents the basic dispersion relationship of the proposed sensor for core and SPP modes of the fundamental y-polarization mode. Here, the CL of the core mode is plotted in primary axis and the real part of the effective index of the core and SPP modes is plotted in secondary axis with respect to the different values of the operational wavelength. It can be seen that at the operating wavelength of $0.87 \mu\text{m}$, the value of effective refractive indices of the core and SPP modes are same with a numerical value of 1.4481, where the maximum CL of 17.2 dB/cm is obtained. This particular wavelength is known as the resonance wavelength where phase matching between the core and SPP modes happens. Due to phase matching state, the maximum energy is being relocated from core to cladding layer and consequences in maximum CL. Figure 6(b), and 6(c) represents the EM field distribution of the core and the SPP modes, respectively.

It should be included that the CL characteristics of the fundamental x-polarization and higher order (TE_{01} and TM_{01}) modes have also been investigated which is shown in Fig-

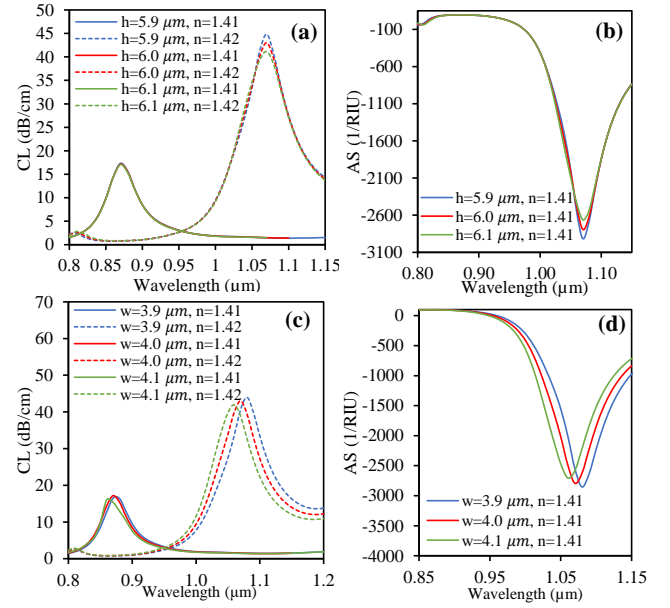


FIGURE 5: CL and AS variation with (a-b) height (h), and (c-d) width (w) of the analyte channel, considering RI of 1.41 and 1.42.

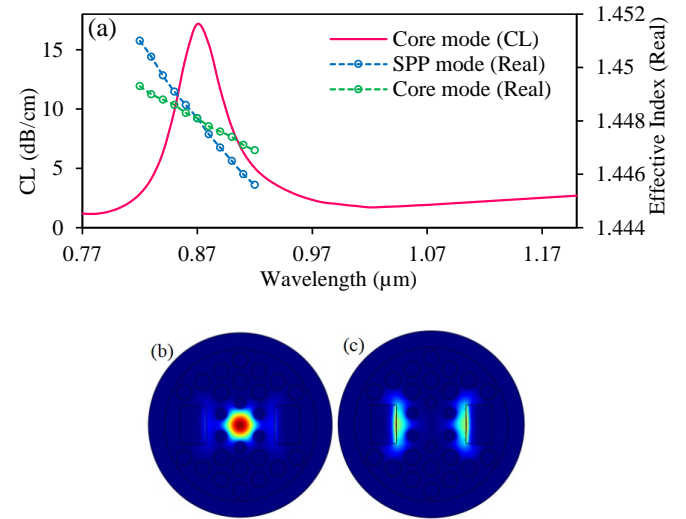


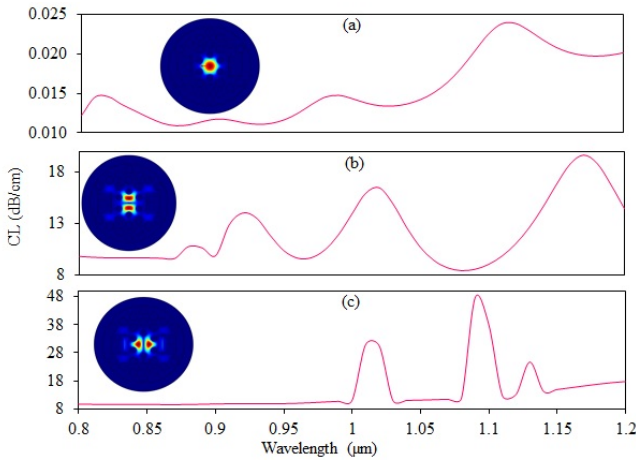
FIGURE 6: (a) Phase matching among the CL, core (real), and SPP (real) mode for an analyte with RI of 1.41, filed distribution of the (b) fundamental y-polarization mode, and (c) SPP mode.

ure 7. In these cases, unlike the fundamental y-polarization mode, multiple loss peaks are obtained at comparatively higher wavelength. Multiple loss peaks for single analyte would increase the complexity in RI sensing, as there is a possibility of interference of one analyte's loss peak with others. However, the fundamental y-polarization mode is considered for further calculation as it provides only one loss peak for each analyte RI.

The EM field that penetrates in between the interface of

TABLE 2: Performance Analysis of the Proposed Sensor for Different Analyte RI With $\Delta n_a = 0.01$ and $t = 30$ nm.

n	CL _{max} (dB/cm)	λ (nm)	$\Delta\lambda$ (nm)	SL (cm)	WS (nm/RIU)	AS (1/RIU)	Resolution (RIU)	FWHM (nm)	SNR (dB)	FOM (1/RIU)	DL (nm)	DA (1/nm)
1.30	0.509	550	10	1.9646	1000	34.89	1×10^{-4}	88	-9.45	11.36	101.05	0.0114
1.31	0.601	560	10	1.6639	1000	41.94	1×10^{-4}	88	-9.45	11.36	101.05	0.0114
1.32	0.725	570	10	1.3793	1000	51.67	1×10^{-4}	84	-9.24	11.91	95.35	0.0119
1.33	0.901	580	10	1.1099	1000	65.68	1×10^{-4}	75	-8.75	13.33	82.75	0.0133
1.34	1.15	590	20	0.8696	2000	85.32	5×10^{-5}	67	-5.25	29.85	60.43	0.0149
1.35	1.45	610	10	0.6897	1000	116.13	1×10^{-4}	56	-7.48	17.86	57.43	0.0179
1.36	1.93	620	30	0.5181	3000	164.35	3.33×10^{-5}	62	-3.15	48.39	49.56	0.0161
1.37	2.70	650	40	0.3704	4000	339.92	2.50×10^{-5}	58	-1.61	68.97	42.43	0.0172
1.38	3.81	690	30	0.2625	3000	298.89	3.33×10^{-5}	53	-2.47	56.60	40.74	0.0189
1.39	5.82	720	60	0.1718	6000	700.61	1.67×10^{-5}	50	0.79	120	31.85	0.0200
1.40	9.50	780	90	0.1053	9000	1334.98	1.11×10^{-5}	49	2.64	183.67	28.06	0.0204
1.41	17.2	870	200	0.0581	20000	2792.97	5.00×10^{-6}	51	5.93	392.16	24.16	0.0196
1.42	43.02	1070	1860	0.0232	186000	102.81	5.38×10^{-7}	85	13.40	2188.24	26.20	0.0118
1.43	293.03	2930	NA	0.0034	NA	NA	NA	NA	NA	NA	NA	NA

FIGURE 7: CL characteristics of the (a) fundamental x-polarization, (b) TE_{01} , and (c) TM_{01} , modes for an analyte with RI of 1.41; corresponding field distribution are shown in the inset.

the metal and the dielectric layer is also known as evanescent field. This evanescent field strikes on the metal surface and frees weakly bounded electrons from the metal and produces surface plasmon wave (SPW). When a small core is used to contain modes and the modes circulates partially out of the core, it introduces a leakage phenomenon results in CL. CL plays a central role for measuring the sensing performance of the sensor and CL is calculated using eqn. 3. The maximum CL (dB/cm) obtained from the numerical analysis are 0.509, 0.601, 0.725, 0.901, 1.150, 1.45, 1.93, 2.70, 3.810, 5.82, 9.50, 17.20, 43 and 298 for a RI of 1.33, 1.34, 1.35, 1.36, 1.37, 1.38, 1.39, 1.40, 1.41, 1.42 and 1.43 respectively and the corresponding resonance wavelength (nm) of the maximum CL are 550, 560, 570, 580, 590, 610, 620, 650, 690, 720, 780, 870, 1070, and 2930, respectively. These data are tabulated in Table 2 and the graphical representation of the CL is plotted in Figure 8 with suitable labeling. From Figure 8, it can be concluded that the peak of the CL shifts from left to right while the value of RI increasing from 1.30 to 1.43

with a step difference of 0.01. Also, the deepness of the CL curve prolongs with larger operating wavelength. Since RI greatly impacts on the effective mode index (n_{eff}), the phase-matching condition also moves to larger wavelength with growing RI.

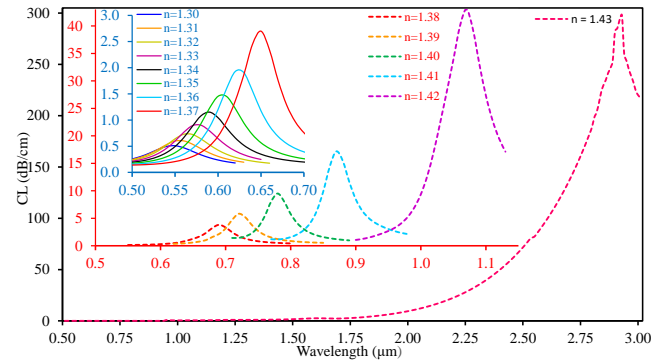


FIGURE 8: Graphical representation of CL for the analyte with RI of 1.30 to 1.43.

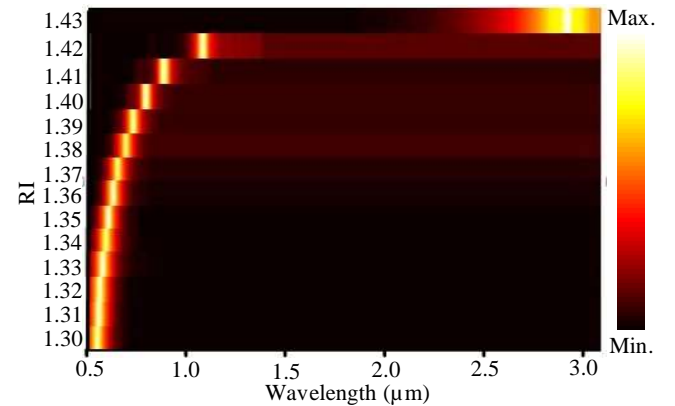


FIGURE 9: Intensity curve of the CL for the analyte with RI of 1.30 to 1.43.

From Figure 8, variation of RI from 1.30 -1.31, 1.31-1.32, 1.32 – 1.33, 1.33 - 1.34, 1.34 – 1.35, 1.35 – 1.36, 1.36 –

1.37, 1.37 – 1.38, 1.38 – 1.39, 1.39 – 1.40, 1.40 – 1.41, 1.41 – 1.42, and 1.42 – 1.43 shifts the resonant wavelength (nm) of 10, 10, 10, 10, 20, 10, 30, 40, 30, 60, 90, 190, and 1860 respectively for y- polarized light. Now using eqn. 4, the corresponding wavelength sensitivities (nm/RIU) are 1000, 1000, 1000, 1000, 2000, 1000, 3000, 4000, 3000, 6000, 9000, 19000, and 186000 respectively and necessary data are recorded in Table 2 sequentially where the the maximum WS (nm/RIU) is 186000 and the average WS (nm/RIU) is 18307.69 having a detection range of RI in-between 1.30 to 1.43. For better understanding, the CL intensity curve is shown in Figure 9 where the CL of the every analyte is normalized by the highest value. However, it can be clearly observed that the loss peak is shifted to the longer wavelength every time the RI increases.

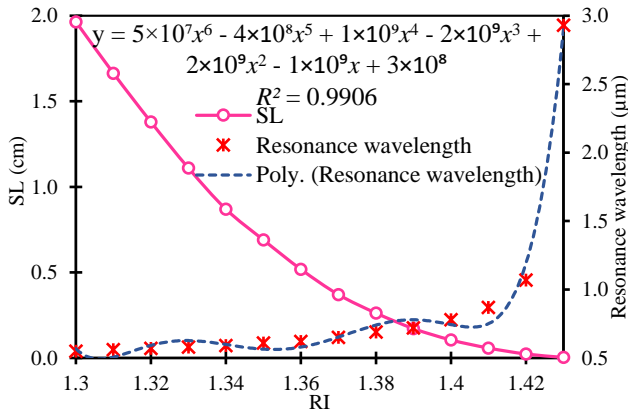


FIGURE 10: Propagation length of the proposed sensor with various RI and resonance wavelength.

The blue dotted line in Figure 10 is the curve fitting of the resonance wavelength. In this proposed sensor, the shift of the resonance wavelength is not exactly linear, hence 6th order polynomial fitting is used instead of linear fitting that provides excellent R^2 (0.9906). The corresponding polynomial equation is shown in eqn. 12.

$$y = 5 \times 10^7 x^6 - 4 \times 10^8 x^5 + 1 \times 10^9 x^4 - 2 \times 10^9 x^3 + 2 \times 10^9 x^2 - 1 \times 10^9 x + 3 \times 10^8 \quad (12)$$

Another parameter which depends directly only on the CL which is SL defined by eqn. 7. From Table 2, it is observed that a rise in RI increases the CL but decreases the SL. Figure 10 shows a graphical presentation of the SL with CL for RI 1.30 to 1.43. From Table 2, the maximum and minimum lengths of the sensor are 1.9646 cm and 34 μm , respectively. Therefore, the propagation length of a sensor can vary between few micron to few centimeter for detecting different RI of analytes.

Wavelength resolution is one more vital directrix and it is applied to measure the possible lowest variation of RI of the analyte that can be identified by the sensor. Utilizing eqn. 5, sensor resolution is being calculated and summarized in Table 2 for RI of 1.30 to 1.42 and it is inversely proportional

to the resonance peak loss. The maximum resolution of the proposed sensor is 5.38×10^{-7} for a RI of 1.42 and it shows that it has a greater capability to detect the change of RI accurately around 10^{-7} or less and more.

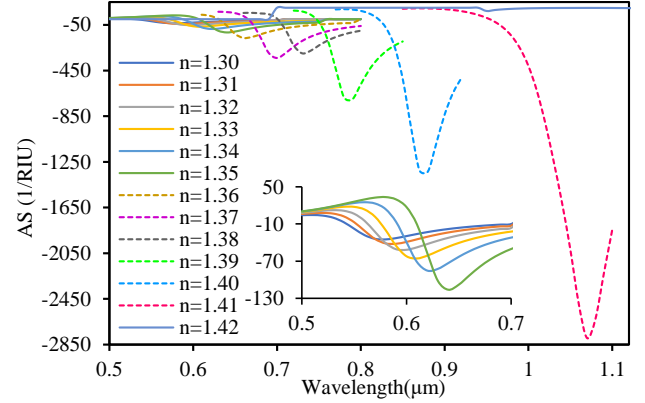


FIGURE 11: AS through graphical depiction for the proposed sensor using different analytes with RI of 1.30 to 1.43.

Apart from WS, AS is an alternative way to represent the performance of the proposed sensor and this parameter has been calculated by means of eqn. 6. From eqn. 6, it can be concluded that AS depends on the CL and necessary numerical data are recorded in Table 2. These data are portrayed in Figure 11 with proper labeling. The highest value of AS is $2792.975 \text{ RIU}^{-1}$ with an operating wavelength of 1070 nm for RI = 1.41 and the average AS is 471.551 RIU^{-1} for RI of 1.30 to 1.42 with a step size of 0.01.

The lower value of FWHM is expected for a sharp peak and it should be as small as possible to avoid false detection. The lower FWHM helps to get higher FOM, SNR, and DA which are calculated using eqn. 8, eqn. 9 and eqn. 11, respectively. From Table 2, it can be seen that the value of FWHM decreases approximately with the increasing value of RI except 1.42. The lowest and highest value of FWHM(nm) are 49 and 88 for RI of 1.40 and both 1.30 and 1.31, respectively. The maximum and minimum SNR(dB) are 13.40 for RI=1.42 and -9.45 for RI of both 1.30 and 1.31. It can be observed that SNR of the proposed sensor increases with the increase of RI. On the other hand, the maximum value of DA is 0.0204 nm^{-1} with RI = 1.40 at which FWHM is minimum and numerical records are tabulated in Table 2. Moreover, FOM is calculated using eqn. 8 and it depends on WS and FWHM. WS increases with the increasing value of RI and FWHM decreases at the same time. After all, FOM increases with the increasing value of RI. From Table 2, the maximum value of FOM is 2188.44 RIU^{-1} for RI = 1.42 with an average FOM of 242.59 RIU^{-1} .

Moreover, a performance comparison has drawn in Table 3 which clearly shows that prior sensors are far behind from our proposed sensor in terms of sensing performance.

TABLE 3: Performance comparison of the proposed dual analyte channel sensor with prior sensors.

RI range	Metal coating	Max. WS (nm/RIU)	Max. AS (RIU ⁻¹)	SNR dB	FOM (RIU ⁻¹)	Resolution (RIU)	Ref.
1.33-1.40	Whole circular outer surface	12,000	933	N/A	217	1.00×10^{-6}	[14]
1.33-1.43	Whole circular outer surface	22,000	1782.56	N/A	64.1	4.56×10^{-6}	[15]
1.377-1.385	Polished flat outer surface	29,000	1030	N/A	1115	3.45×10^{-5}	[20]
1.3-1.412	Circular outer surface	50,000	1449	N/A	335	2.00×10^{-6}	[22]
1.32-1.36	Polished outer flat surface and split air holes	2331.9	200.7	N/A	N/A	8.55×10^{-6}	[35]
1.373-1.402	Whole circular outer surface	14,285.71	N/A	N/A	N/A	N/A	[36]
1.25-1.43	Outer U-shaped groove	13,200	5440	N/A	527	1.47×10^{-5}	[37]
1.33-1.45	Outer circular slot	38,000	1286	N/A	760	2.63×10^{-6}	[38]
1.33-1.42	Whole circular outer surface	20,000	1380	2.21	470	5.26×10^{-6}	[39]
1.33-1.36	Inner circular segment	10,600	633.4	N/A	303	9.43×10^{-6}	[24]
1.30-1.43	Inner flat surface	186,000	2792.97	13.4	2188.24	5.38×10^{-7}	Proposed design

V. CONCLUSION

In this study, a novel dual channel PCF-SPR is proposed and analyzed the performance using FEM. The challenge associated with the metal coating for SPR-PCF sensor is attempted to be overcome by the metal deposition on the flat surface of the analyte channels, which placed really close to the core so that SPs can be excited effectively. Thus, the sensing performance as well as sensing range is improved significantly. The sensor shows WS and AS of 186,000 nm/RIU and 2,792.97 RIU⁻¹, respectively, and subsequently high resolution, excellent FOM, DA, and DL. Due to the highly sensitive feature, the proposed sensor could be effectively used practically in the bio sensing field.

REFERENCES

- [1] T. A. Birks, J. C. Knight, and P. S. J. Russell, "Endlessly single-mode photonic crystal fiber," *Optics letters*, vol. 22, pp. 961-963, 1997.
- [2] J. Homola, S. S. Yee, and G. Gauglitz, "Surface plasmon resonance sensors," *Sensors and actuators B: Chemical*, vol. 54, pp. 3-15, 1999.
- [3] D. J. J. Hu and H. P. Ho, "Recent advances in plasmonic photonic crystal fibers: design, fabrication and applications," *Advances in Optics and Photonics*, vol. 9, pp. 257-314, 2017.
- [4] A. K. Sharma, R. Jha, and B. Gupta, "Fiber-optic sensors based on surface plasmon resonance: a comprehensive review," *IEEE Sensors Journal*, vol. 7, pp. 1118-1129, 2007.
- [5] T. Wieduwilt, A. Tuniz, S. Linzen, S. Goerke, J. Dellith, U. Hübner, et al., "Ultrathin niobium nanofilms on fiber optical tapers—a new route towards low-loss hybrid plasmonic modes," *Scientific reports*, vol. 5, pp. 1-12, 2015.
- [6] P. B. Johnson and R.-W. Christy, "Optical constants of the noble metals," *Physical review B*, vol. 6, p. 4370, 1972.
- [7] M. A. Ordal, R. J. Bell, R. W. Alexander, L. L. Long, and M. R. Query, "Optical properties of fourteen metals in the infrared and far infrared: Al, Co, Cu, Au, Fe, Pb, Mo, Ni, Pd, Pt, Ag, Ti, V, and W," *Applied optics*, vol. 24, pp. 4493-4499, 1985.
- [8] P. R. West, S. Ishii, G. V. Naik, N. K. Emani, V. M. Shalae, and A. Boltasseva, "Searching for better plasmonic materials," *Laser 'l&' Photonics Reviews*, vol. 4, pp. 795-808, 2010.
- [9] B. Shuai, L. Xia, and D. Liu, "Coexistence of positive and negative refractive index sensitivity in the liquid-core photonic crystal fiber based plasmonic sensor," *Optics express*, vol. 20, pp. 25858-25866, 2012.
- [10] D. Gao, C. Guan, Y. Wen, X. Zhong, and L. Yuan, "Multi-hole fiber based surface plasmon resonance sensor operated at near-infrared wavelengths," *Optics Communications*, vol. 313, pp. 94-98, 2014.
- [11] A. A. Rifat, F. Haider, R. Ahmed, G. A. Mahdiraji, F. M. Adikan, and A. E. Miroshnichenko, "Highly sensitive selectively coated photonic crystal fiber-based plasmonic sensor," *Optics letters*, vol. 43, pp. 891-894, 2018.
- [12] A. K. Paul, A. K. Sarkar, A. B. S. Rahman, and A. Khaleque, "Twin core photonic crystal fiber plasmonic refractive index sensor," *IEEE Sensors Journal*, vol. 18, pp. 5761-5769, 2018.
- [13] M. S. Islam, J. Sultana, A. A. Rifat, R. Ahmed, A. Dinovitser, B. W.-H. Ng, et al., "Dual-polarized highly sensitive plasmonic sensor in the visible to near-IR spectrum," *Optics express*, vol. 26, pp. 30347-30361, 2018.
- [14] F. Haider, R. A. Aoni, R. Ahmed, W. J. Chew, and G. A. Mahdiraji, "Alphabetic-Core Assisted Microstructure Fiber Based Plasmonic Biosensor," *Plasmonics*, vol. 15, pp. 1949-1958, 2020.
- [15] H. Sarker, M. Faisal, and M. A. Mollah, "Slotted photonic crystal fiber-based plasmonic biosensor," *Applied Optics*, vol. 60, pp. 358-366, 2021.
- [16] A. A. Rifat, M. R. Hasan, R. Ahmed, and A. E. Miroshnichenko, "Microstructured optical fiber-based plasmonic sensors," *Computational Photonic Sensors*, ed: Springer, 2019, pp. 203-232.
- [17] A. A. Rifat, R. Ahmed, G. A. Mahdiraji and F. R. M. Adikan, "Highly Sensitive D-Shaped Photonic Crystal Fiber-Based Plasmonic Biosensor in Visible to Near-IR," in *IEEE Sensors Journal*, vol. 17, no. 9, pp. 2776-2783, 1 May 2017, doi: 10.1109/JSEN.2017.2677473.
- [18] R. K. Gangwar and V. K. Singh, "Highly sensitive surface plasmon resonance based D-shaped photonic crystal fiber refractive index sensor," *Plasmonics*, vol. 12, pp. 1367-1372, 2017.
- [19] X. Chen, L. Xia, and C. Li, "Surface plasmon resonance sensor based on a novel D-shaped photonic crystal fiber for low refractive index detection," *IEEE Photonics Journal*, vol. 10, pp. 1-9, 2018.
- [20] X. Meng, J. Li, Y. Guo, S. Li, S. Zhang, Y. Liu, et al., "Analysis of Double Peak Detection in a D-Shaped Photonic Crystal Fiber Plasmonic Sensor," *Plasmonics*, pp. 1-8, 2021.
- [21] M. S. Islam, C. M. Cordeiro, J. Sultana, R. A. Aoni, S. Feng, R. Ahmed, et al., "A Hi-Bi ultra-sensitive surface plasmon resonance fiber sensor," *IEEE access*, vol. 7, pp. 79085-79094, 2019.
- [22] M. A. Mollah and M. S. Islam, "Novel single hole exposed-suspended core localized surface plasmon resonance sensor," *IEEE Sensors Journal*, vol. 21, pp. 2813-2820, 2020.
- [23] M. S. Islam, M. R. Islam, J. Sultana, A. Dinovitser, B. W.-H. Ng, and D. Abbott, "Exposed-core localized surface plasmon resonance biosensor," *JOSA B*, vol. 36, pp. 2306-2311, 2019.
- [24] H. Fang, C. Wei, D. Wang, L. Yuan, S. Jiao, Z. Bao, et al., "Research on photonic crystal fiber based on a surface plasmon resonance sensor with segmented silver-titanium dioxide film," *JOSA B*, vol. 37, pp. 736-744, 2020.
- [25] M. S. Islam, C. M. Cordeiro, M. A. Franco, J. Sultana, A. L. Cruz, and D. Abbott, "Terahertz optical fibers," *Optics express*, vol. 28, pp. 16089-16117, 2020.
- [26] P. J. Sazio, A. Amezcua-Correa, C. E. Finlayson, J. R. Hayes, T. J. Scheidemantel, N. F. Baril, et al., "Microstructured optical fibers as high-pressure microfluidic reactors," *Science*, vol. 311, pp. 1583-1586, 2006.
- [27] S. Randolph, J. Fowlkes, and P. Rack, "Focused electron-beam-induced etching of silicon dioxide," *Journal of applied physics*, vol. 98, p. 034902, 2005.
- [28] J. Boehm, A. François, H. Ebendorff-Heidepriem, and T. M. Monro, "Chemical deposition of silver for the fabrication of surface plasmon microstructured optical fibre sensors," *Plasmonics*, vol. 6, pp. 133-136, 2011.
- [29] X. Zhang, R. Wang, F. Cox, B. Kuhlmeier, and M. Large, "Selective coating of holes in microstructured optical fiber and its application to in-fiber absorptive polarizers," *Optics Express*, vol. 15, pp. 16270-16278, 2007.
- [30] A. Wang, A. Docherty, B. T. Kuhlmeier, F. M. Cox, and M. C. Large, "Side-hole fiber sensor based on surface plasmon resonance," *Optics letters*, vol. 34, pp. 3890-3892, 2009.

- [31] E. Klantsataya, A. François, H. Ebendorff-Heidepriem, P. Hoffmann, and T. M. Monro, "Surface plasmon scattering in exposed core optical fiber for enhanced resolution refractive index sensing," *Sensors*, vol. 15, pp. 25090-25102, 2015.
- [32] H. E. Arabi, M. Pournoury, J. H. Park, S. Im, and K. Oh, "Plasmonically enhanced optical transmission through a metalized nanostructured photonic crystal fiber taper," *Optics letters*, vol. 36, pp. 2029-2031, 2011.
- [33] F. Haider, M. Mashrafi, R. A. Aoni, R. Haider, M. Hossen, T. Ahmed, et al., "Multi-Analyte Detection Based on Integrated Internal and External Sensing Approach," *IEEE Transactions on NanoBioscience*, 2021.
- [34] S. Jiao, X. Ren, H. Yang, S. Xu, and X. Li, "Dual-Channel and Dual-Core Plasmonic Sensor-Based Photonic Crystal Fiber for Refractive Index Sensing," *Plasmonics*, pp. 1-10, 2021.
- [35] W. Luo, X. Li, J. Meng, Y. Wang, and X. Hong, "Surface plasmon resonance sensor based on side-polished D-shaped photonic crystal fiber with split cladding air holes," *IEEE Transactions on Instrumentation and Measurement*, vol. 70, pp. 1-11, 2021.
- [36] V. S. Chaudhary, D. Kumar, and S. Kumara, "Gold-immobilized Photonic Crystal Fiber-based SPR Biosensor for Detection of Malaria Disease in Human Body," *IEEE Sensors Journal*, 2021. DOI:10.1109/JSEN.2021.3085829
- [37] H. Wang, W. Rao, J. Luo, and H. Fu, "A Dual-Channel Surface Plasmon Resonance Sensor Based on Dual-Polarized Photonic Crystal Fiber for Ultra-Wide Range and High Sensitivity of Refractive Index Detection," *IEEE Photonics Journal*, vol. 13, pp. 1-11, 2021.
- [38] N. Sakib, W. Hassan, Q. Kamrunnahar, M. Momtaj, and T. Rahman, "Dual core four open channel circularly slotted gold coated plasmonic biosensor," *Optical Materials Express*, vol. 11, pp. 273-288, 2021.
- [39] N. Jahan, M. M. Rahman, M. Ahsan, M. A. Based, M. M. Rana, S. Gurusamy, et al., "Photonic Crystal Fiber Based Biosensor for Pseudomonas Bacteria Detection: A Simulation Study," *IEEE Access*, vol. 9, pp. 42206-42215, 2021.



MD. ASLAM MOLLAH is an Assistant Professor of Electronics and Telecommunication Engineering at Rajshahi University of Engineering and Technology. He received his B.Sc degree in Electronics and Telecommunication Engineering (ETE) and M.Sc degree in Electrical and Electronic Engineering (EEE) from the same institution. He is a graduate member of IEEE. His research interests include optical fiber communication, PCF based terahertz waveguides, terahertz sensors, surface plasmon resonance biosensors. Mr. Mollah published 21 peer-reviewed articles and actively reviews for IEEE JOURNAL OF LIGHT-WAVE TECHNOLOGY, Optics Express, JOSA B, Applied Optics, OSA Continuum, ACS Applied Nano Materials, Optical Fiber Technology, and Optik etc.



HASAN SARKER was born in Comilla, Bangladesh in 1992. He has received his B.Sc. Engineering degree from the Department of Electronics and Telecommunication Engineering (ETE) from Rajshahi University of Engineering and Technology (RUET), Bangladesh in 2016. He has joined as a lecturer with the dept. of ETE at RUET in 2019 and currently he is pursuing his M.Sc. in Engineering degree from the Department of Electrical and Electronic Engineering (EEE) from Bangladesh University of Engineering and Technology (BUET), Bangladesh. His research concentration encircles PCF based plasmonic biosensor, optical fiber communication and optical sensor and devices.



DR MOMINUL AHSAN is currently working as an Associate Lecturer in the Department of Computer Science, University of York, UK. He has worked as a Postdoctoral Researcher in the Department of Engineering, Manchester Met University before joining at University of York. He completed his Ph.D. degree in 2019 from the School of Computing and Mathematical Sciences at the University of Greenwich, London, UK. Mr. Ahsan has obtained his MEng degree (Research) from the Faculty of Engineering and Computing at Dublin City University, Dublin, Ireland in 2014 and a B.Sc. Degree from the Department of Computer Science and Engineering at State University of Bangladesh, Dhaka, Bangladesh in 2008. His research interests include prognostics, data analytics, machine learning, reliability, power electronics, wireless communication, and wearable technology. Dr Ahsan is currently a Member of the Institution of Engineering and Technology (MIET) UK, Associate Fellow of Higher Education Academy (AFHEA) UK, and Associate Member of Bangladesh Computer Society. He is also a recipient of MEng stipend at Dublin City University in 2010, PhD VC scholarship at University of Greenwich in 2014, and Excellent Poster Award in the IEEE International Spring Seminar on Electronic Technology at Sofia, Bulgaria in 2017.



MD. TOWFIK ELAHI was born in Nawabganj, Bangladesh. He is pursuing his B.Sc. Engineering degree from the Department of Electronics and Telecommunication Engineering (ETE) from Rajshahi University of Engineering and Technology (RUET), Bangladesh.



MD. ABDUL BASED (IEEE MEMBER) was born in Nilphamari, Bangladesh in 1979. He received the B.S. degree in Computer Science and Engineering from Dhaka International University, Dhaka, Bangladesh in the year 2000. His first M.S. degree is in Computer Science from North South University in the year 2005. His second M.S. degree is received in Information and Communication Systems Security (ICSS) from the Royal Institute of Technology (KTH) in the year 2008. From 2008 to 2014, he worked as a Research Fellow at the Norwegian University of Science and Technology (NTNU), Trondheim, Norway on the security aspects of electronic voting. Since 2014, he has been an Associate Professor with the Electrical, Electronics and Telecommunication Engineering (EETE) Department, Dhaka International University, Dhaka, Bangladesh. He also worked as the Head of Computer Science and Engineering Department at the same university. Since 1st September, 2019 he has been working as the head of EETE (recently renamed as EEE) Department at Dhaka International University. Besides teaching and research, he also worked as IT and MIS Specialist in a Government Project at Ministry of Planning, Dhaka, Bangladesh. He is an expert of Curriculum Design and Development, and Outcome Based Education. His research interests include information security, electronic voting and cryptographic protocols. Associate Professor Based is a life-time member as well as elected councilor of Bangladesh Computer Society (BCS) [2018-2020], Bangladesh.



DR JULFIKAR HAIDER is currently working as a Senior Lecturer in Mechanical Engineering at the Department of Engineering, Manchester Metropolitan University, UK. Dr Haider's main research is Materials Processing, thin film coating, composite materials, Finite element analysis, and Artificial intelligence; and it is in these areas that he is renowned for his work both Nationally and Internationally justified by his research outputs in International journals and conferences. He has been supervising research associates and PhD students in the above areas. He has published and presented over 100 technical papers in international journals, conferences and books. He is acting as the Executive Editor for an International Journal published by Taylor and Francis (Advances in Materials and Processing Technologies). He has received funding from Innovate UK to conduct Eight Knowledge Transfer Partnership projects with industry worth more than a million pound.



DR SIVAPRAKASAM PALANI received B.E. degree in Industrial Engineering (2005), M.E. Degree in Computer Integrated Manufacturing (2008) and Ph.D. Degree in Mechanical Engineering (2015) from College of Engineering Guindy, Anna University, Chennai, India. At present Dr Palani is working as Associate Professor in Addis Ababa Science and Technology University, Ethiopia. His research interest includes Micro/nano Manufacturing, Machining, Composite Materials, Surface Engineering and Optimization Techniques. He has 13 years of teaching and research experience including international teaching experience in Oman and Ethiopia. He has published papers in 22 International Journals and 18 International/National conferences.

...